Supplementary Information for: Accelerated destabilization of transportation networks across the Northern Hemisphere by permafrost-infrastructure interactions

Rui Chen[1,2], Jan Nitzbon[1,3], Haoying Li[2], and Moritz Langer[1,4]

[1]Permafrost Research Section, Alfred Wegener Institute Helmholtz Centre for Polar and Marine Research, Potsdam, Germany
[2]Geography Department, Humboldt-Universität zu Berlin, Berlin, Germany
[3]Geographical Institute, Georg-August-Universiät Göttingen, Göttingen, Germany
[4]Faculty of Science, Vrije Universiteit Amsterdam, Amsterdam, The Netherlands

Corresponding author: Rui Chen (rui.chen@awi.de)

Supplementary Text 1: Adjustment of incoming solar radiation on the embankment shoulder

To account for the incoming solar radiation received on the embankment slope at each simulated grid cell, we computed the solar azimuth and elevation angle from Coordinated Universal Time and geographic coordinates (longitude, latitude, and altitude). The position of the Sun was estimated using a simplified astronomical algorithm[1] incorporating the Julian date, orbital parameters of Earth, and the obliquity of the ecliptic. The right ascension and declination of the Sun were derived from its ecliptic coordinates, and the solar elevation was determined in the local horizontal coordinate system. The correction factor (G) for slope inclination and orientation was calculated as:

$$G = \frac{\cos(\alpha)\sin(\beta)\cos(\psi - \theta) + \sin(\alpha)\cos(\beta)}{\sin(\alpha)} \tag{1}$$

where α is the solar elevation angle, β is the embankment slope angle, θ is the solar azimuth angle, and ψ is the azimuth angle of the embankment slope, which is determined by the embankment direction. In our study, we considered that $\psi = 0°$ or $180°$ when the embankment shoulder faces towards North or South in the Northern Hemisphere.

The factor G was set to zero when $\alpha <= 0°$ or $G < 0$, and the incoming shortwave radiation on slope was then corrected as:

$$S_{slope} = S_{in} \cdot G \tag{2}$$

where S_{in} is the incoming shortwave radiation from the forcing data. S_{slope} represents the effective solar radiation reaching the inclined surface.

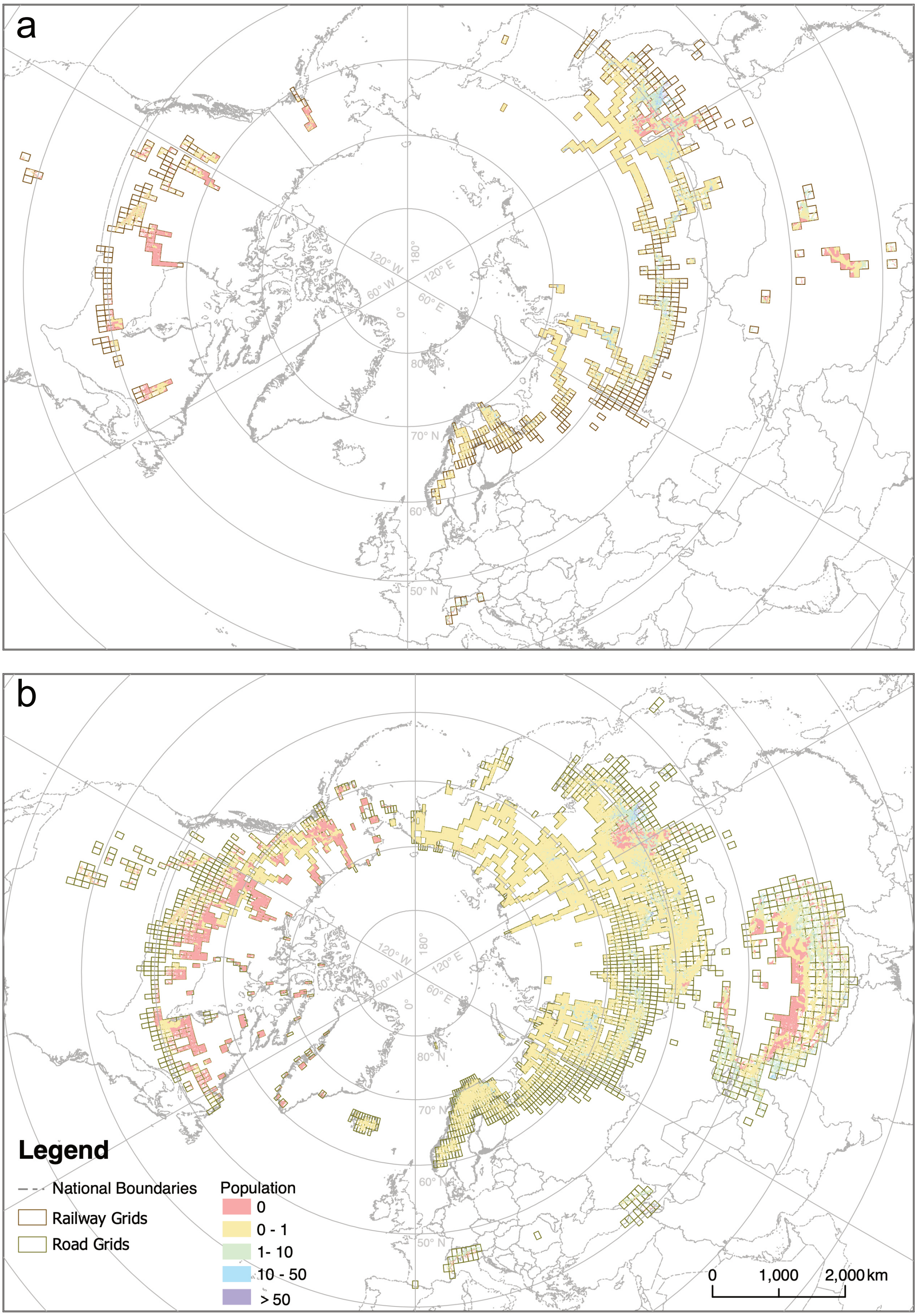

Supplementary Fig. 1: Spatial distribution of population in 2000 in the modelled roads and railways grid cells across the Northern Hemisphere permafrost areas. **a,** Railway. **b** Road. The population data are obtained from ref.2

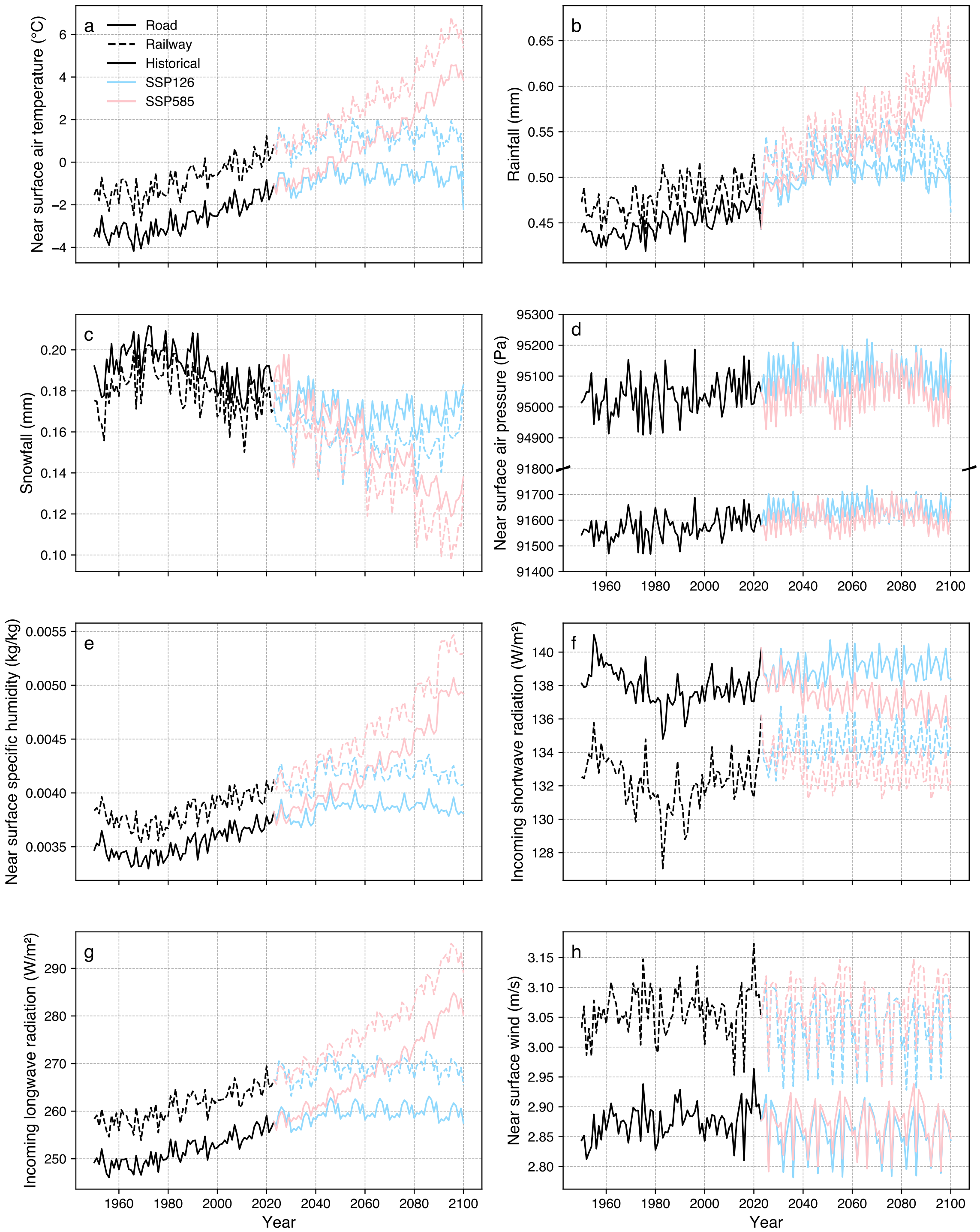

Supplementary Fig. 2: Timeseries of forcing variables (**a**, surface air temperature, **b**, rainfall, **c**, snowfall, **d**, specific humidity, **e**, surface air pressure, **f**, incoming shortwave radiation, **g**, incoming longwave radiation, and **h**, wind speed during 1950–2100 over the roads and railways grid-cells under two different scenarios from MPI-ESM1-2-HR Earth system model.

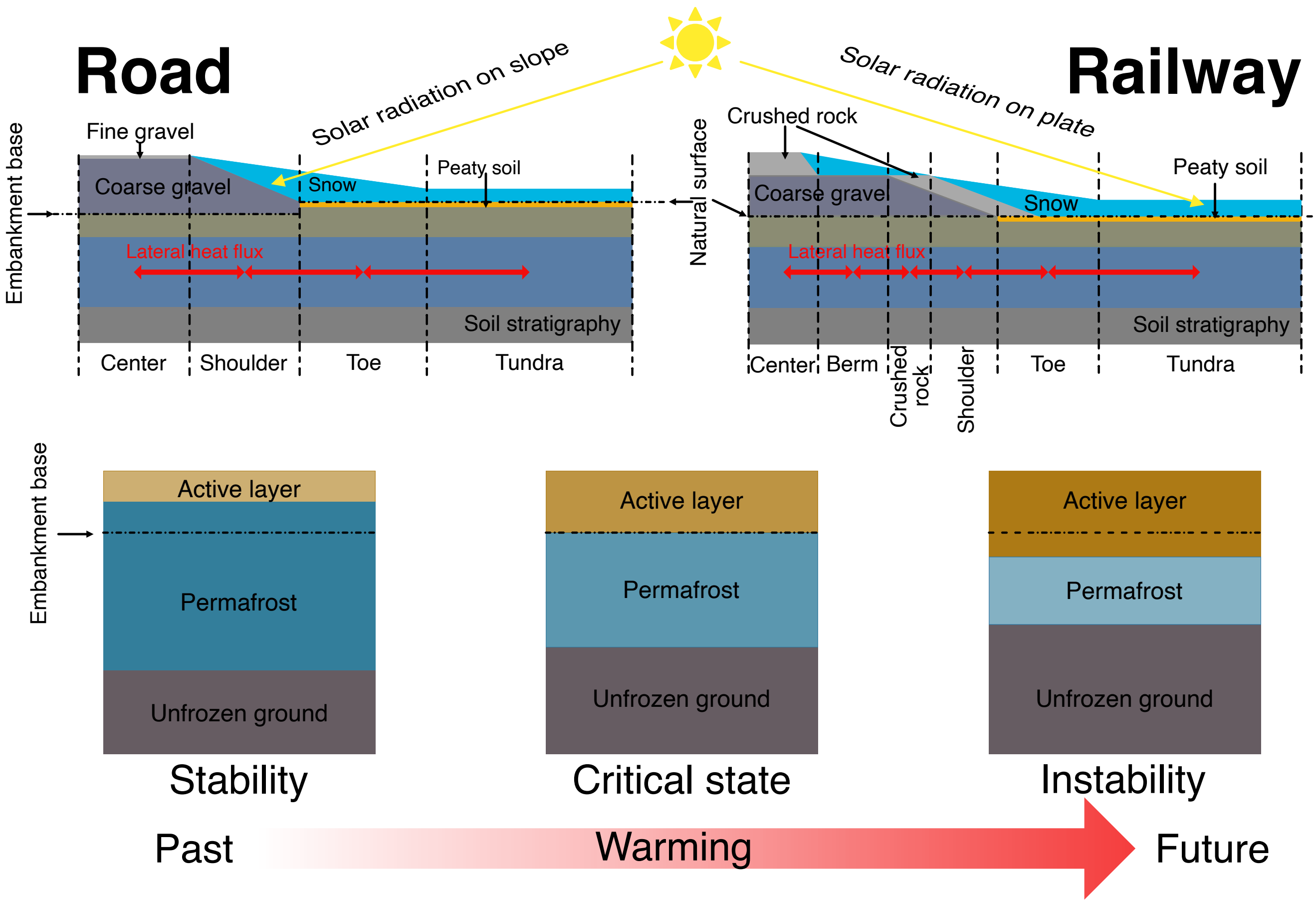

Supplementary Fig. 3: Schematic for modelled half cross-section from the transportation infrastructure centre to the adjacent tundra

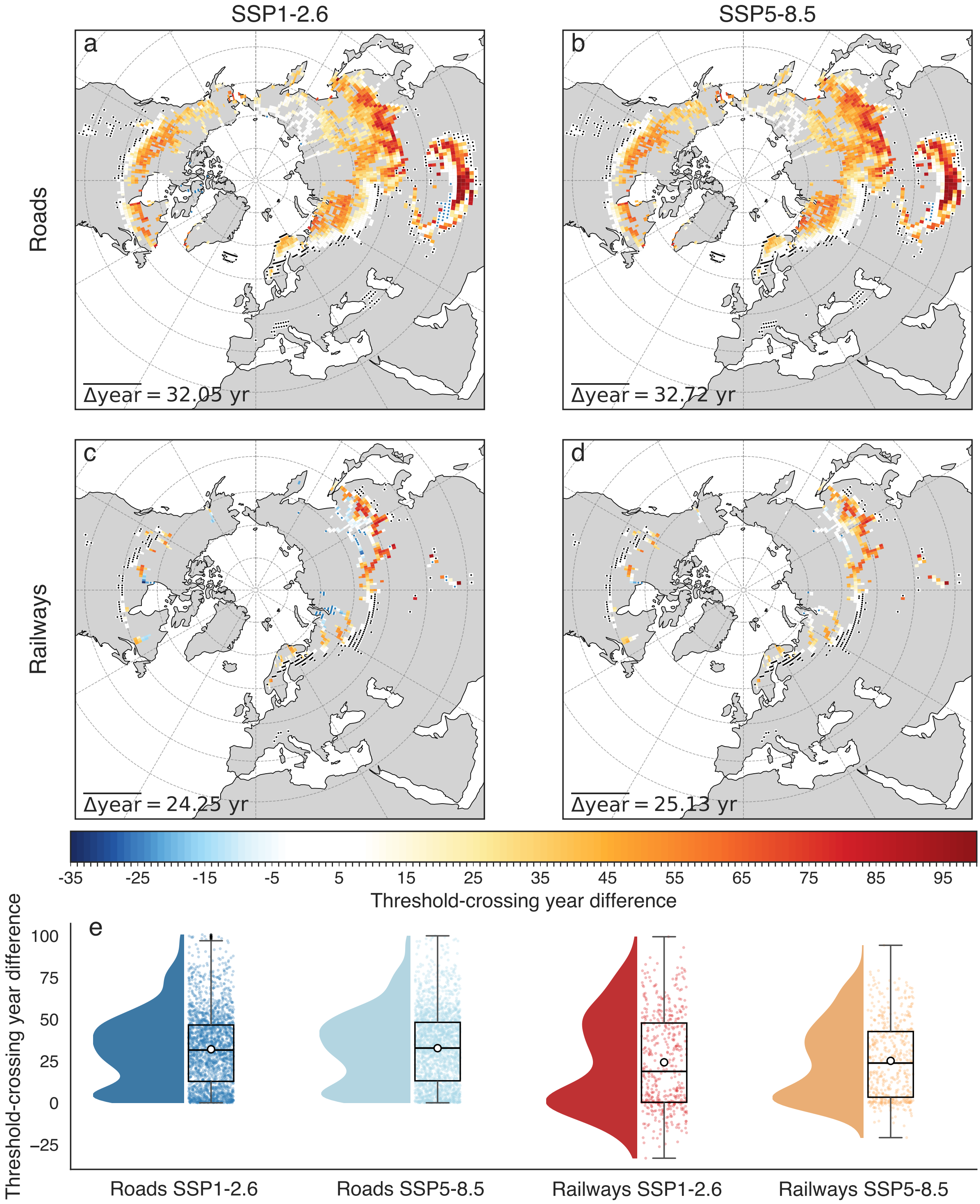

Supplementary Fig. 4: Time difference between the annual maximum thaw depth of transportation infrastructure and natural ground reaches 5 m. **a-d**, Spatial patterns of the ensemble mean and latitudinal distribution of the difference between roads and adjacent natural ground. **c-d**, same as **a-b**, but for railways. Numbers in the right corner of each panel indicate ensemble means. Black (MTD reached 5 m in 2000 for both embankment and natural ground units) and blue (MTD unreached 5 m in 2100 for both embankment and natural ground units) dots mark grid cells with no projected change.**e**, Raincloud plot summarizing the distribution of time differences across all 1°×1° grid cells within the model domain. Whiskers extend to 1.5×interquartile range; boxes represent the interquartile range (25th to 75th percentiles); the black centre line and white dot indicate the median and mean value, respectively. Black (MTD has penetrated the threshold depth in 2000) and blue (MTD has not penetrated the threshold depth in 2100) dots mark grid cells with no projected change. Values in the low-right corner of each panel report the average over grid cells of the time difference and are computed over grid cells with a change only.

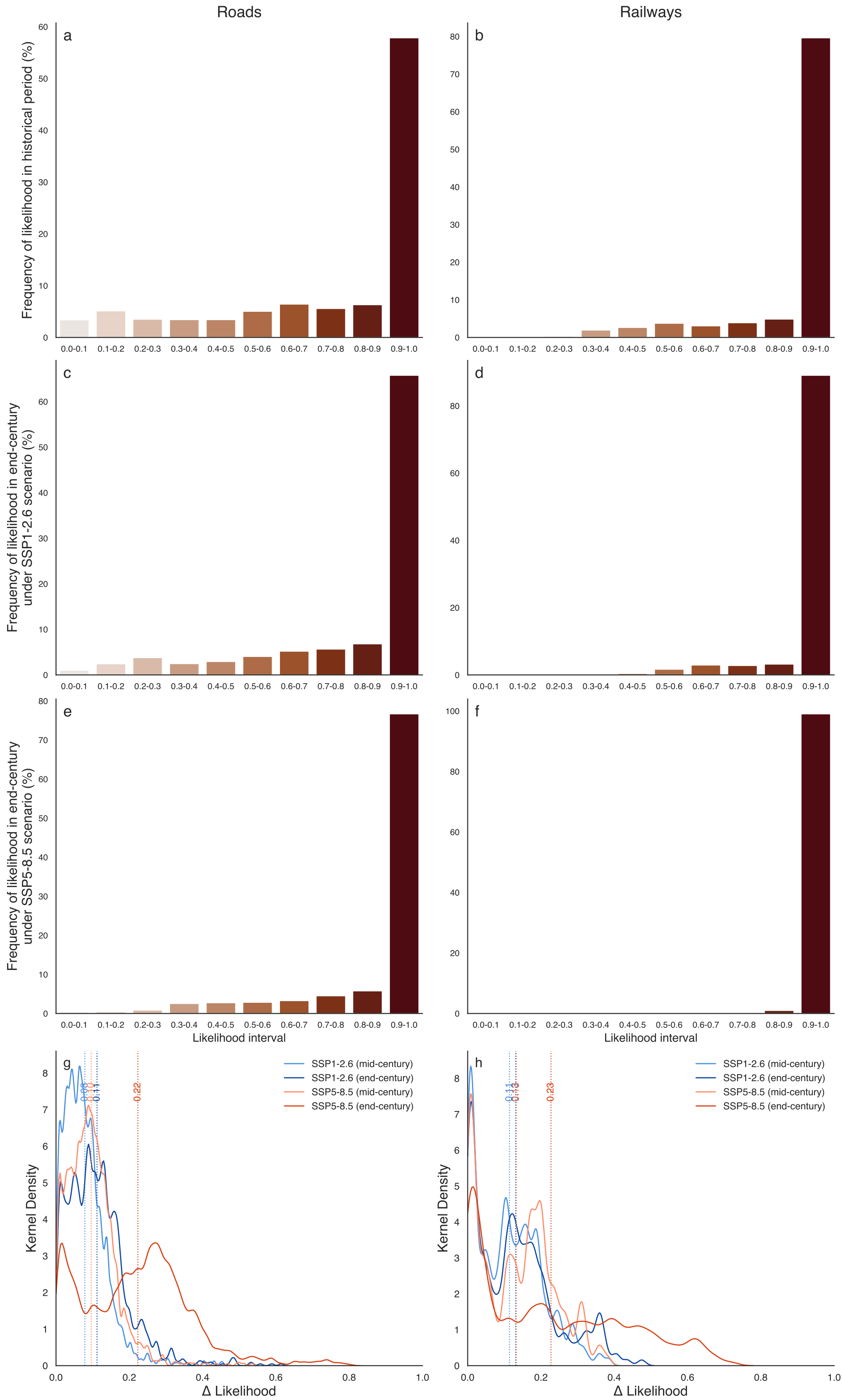

Supplementary Fig. 5: Frequency of likelihood in different periods for roads and railways. **a, b**, Historical period (2000–2023). **c, d**, End-century (2081–2100) under SSP1–2.6 scenarios. **e, f** same as **c-d**, but for SSP5–8.5. **g,h**, Kernel density of grid-cell $\Delta LPTI$ for roads and railways in mid-century and end-century under SSP1–2.6 and SSP5–8.5 scenarios.

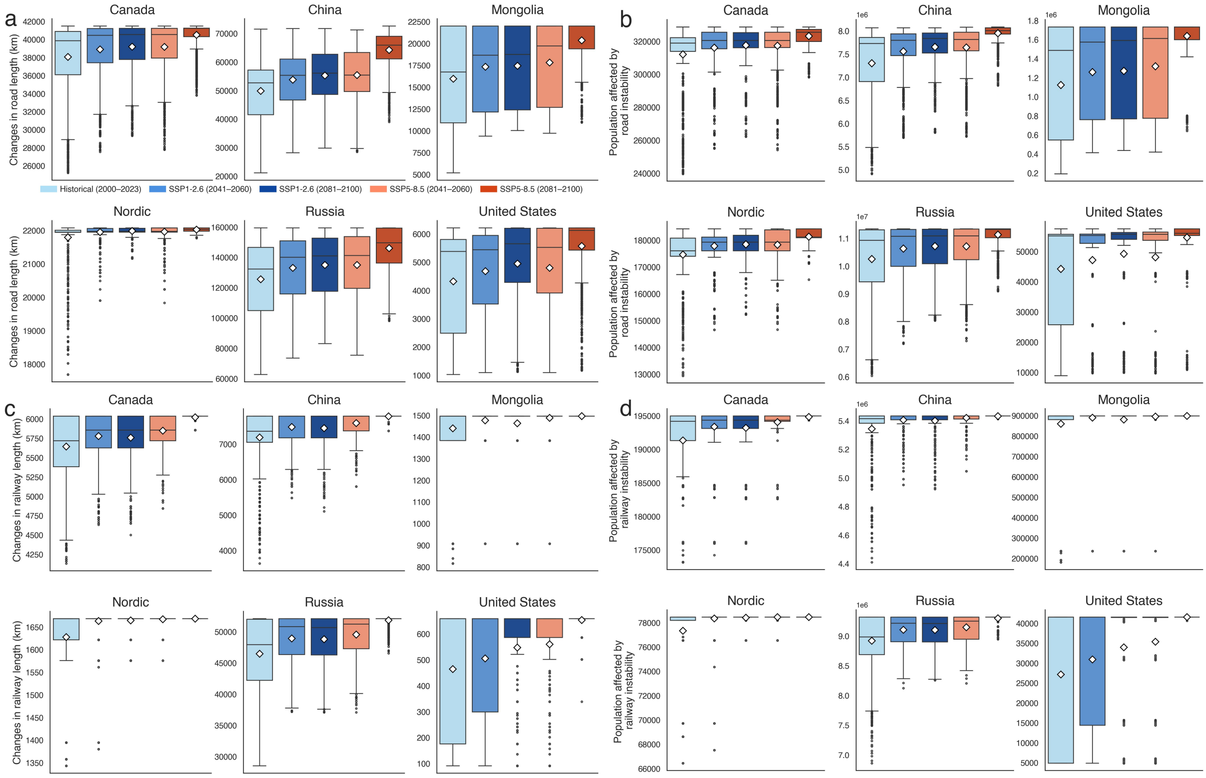

Supplementary Fig. 8 Changes in the length of unstable transportation infrastructure and population it serves in different countries and regions. **a, b**, box plot of the length of unstable roads and it served population in three periods under two climate scenarios. **c, d**, same as **a, b**, but for railways.

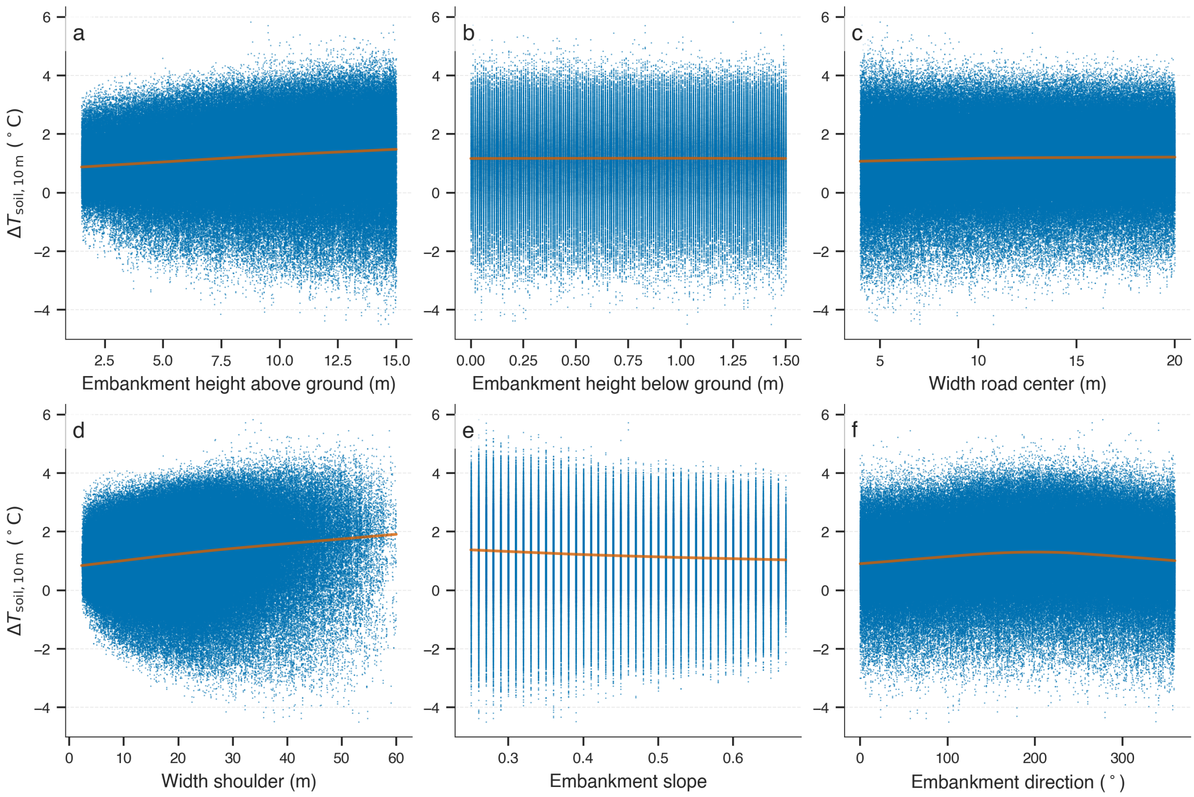

Supplementary Fig. 9 Ensemble sensitivity of $\Delta_{MAGT10m}$ to embankment geometry for roads. **a**, Embankment height above ground (m). **b**, Embankment height below ground (m). **c**, Width of road center (m). **d**, Width of road shoulder (m). **e**, Embankment slope (dimensionless). **f**, Embankment direction (°).

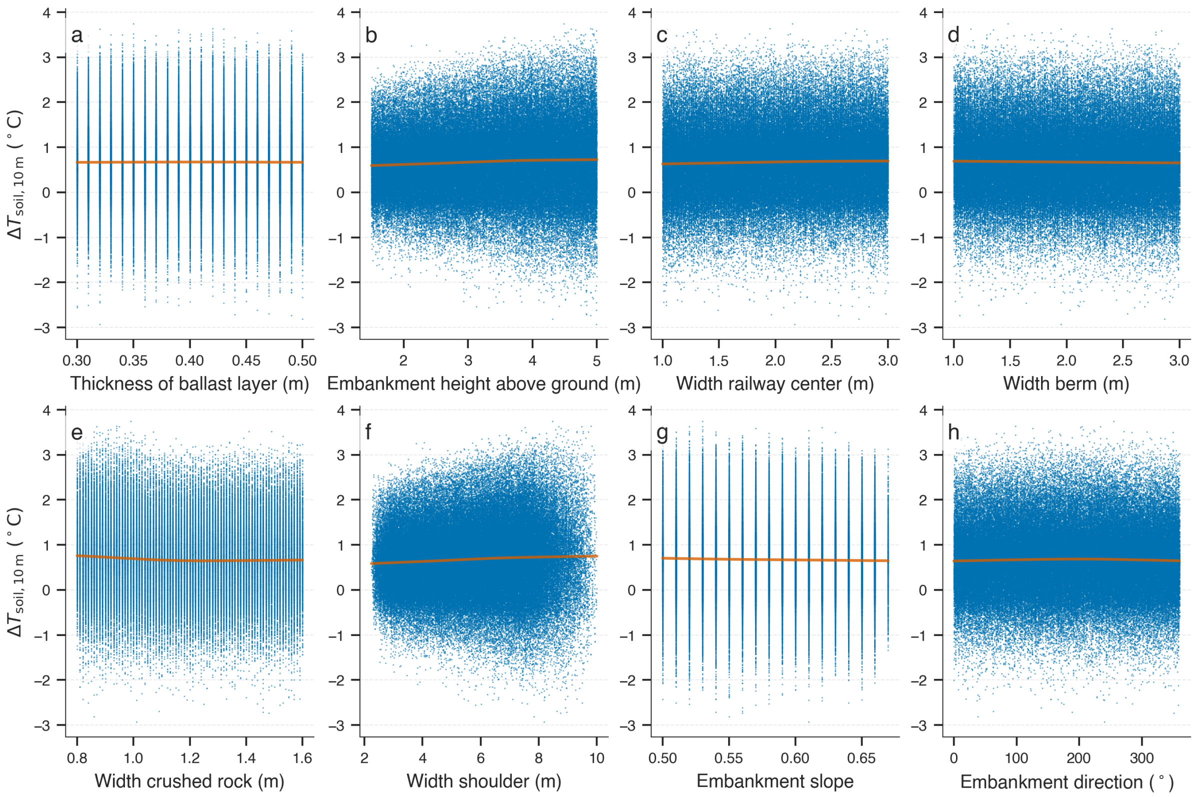

Supplementary Fig. 10 Ensemble sensitivity of $\Delta_{MAGT10m}$ to embankment geometry for railways. **a**, Thickness of ballast layer (m). **b**, Embankment height above ground (m). **c**, Width of railway center (m). **d**, Width of railway berm (m). **e**, Width of crushed-rock (m). **f**, Width of shoulder (m). **g**, Embankment slope (dimensionless). **h** Embankment direction (°).

Supplementary Table 1: Summary of road lengths in different permafrost zones by country

Country	Isolated	Sporadic	Discontinuous	Continuous
Afghanistan	255.68	20.89	—	—
Armenia	16.10	7.06	2.69	—
Austria	114.74	32.87	3.63	—
Azerbaijan	19.00	22.50	9.62	—
Bhutan	28.81	24.50	18.95	25.79
Canada	28 765.92	6829.58	2944.16	2942.43
China	25 422.36	19 105.09	11 687.28	16 160.32
Denmark	29.62	41.46	19.72	62.16
Finland	6431.07 550.92	0.97	—	
France	81.43	47.24	2.70	—
Georgia	44.21	23.63	7.86	—
Iceland	1153.67	719.17	6.50	—
India	1138.46	465.29	231.68	126.93
Italy	203.49	52.05	0.69	—
Japan	13.03	—	—	—
Kazakhstan	250.54	29.75	22.67	2.66
Kyrgyzstan	497.37	528.82	713.34	281.83
Mongolia	8108.22	5895.26	5591.76	2375.40
Nepal	39.29	39.25	10.58	—
North Korea	137.17	10.84	8.06	—
Norway	4104.10	582.59	0.54	24.12
Pakistan	314.92	35.51	8.75	3.89
Romania	6.50	0.21	—	—
Russia	84 338.24	33 136.60	12 087.49	29 901.14
Sweden	7810.79	532.58	—	—
Switzerland	267.70	69.72	—	—
Tajikistan	455.60	214.15	15.50	—
Turkey	110.56	39.97	—	—
United States	1445.28	2231.18	1345.95	1193.44
Uzbekistan	0.92	—	—	—

Supplementary Table 2: Summary of railway lengths in different permafrost zones by country

Country	Isolated	Sporadic	Discontinuous	Continuous
Austria	12.20	7.46	2.21	—
Canada	4542.73	942.39	339.55	210.14
China	2654.11	3000.46	1068.44	1022.53
Finland	219.47	—	—	—
France	2.78	4.22	—	—
Italy	6.47	8.78	1.80	—
Kazakhstan	48.88	—	—	—
Mongolia	850.30	406.29	238.99	—
North Korea	26.24	—	—	—
Norway	169.63	9.78	—	—
Russia	30 896.56	12 129.34	5787.91	3269.44
Sweden	1036.88	232.61	—	—
Switzerland	49.81	67.27	4.26	—
United States	199.85	341.00	111.84	6.01

Supplementary Table 3: Population with road access by country: A spatial analysis based on WorldPop data and 1-degree grid cells

Country	Population
Afghanistan	142 630
Armenia	944
Austria	36 720
Azerbaijan	21 847
Bhutan	5435
Canada	328 623
China	7 256 193
Denmark	17 306
Finland	41 289
France	13 183
Georgia	14 367
Germany	720
Iceland	6981
India	476 900
Italy	4018
Japan	4130
Kazakhstan	78 665
Kyrgyzstan	290 583
Liechtenstein	97
Mongolia	1 363 520
Myanmar	699
Nepal	73 324
North Korea	39 025
Norway	68 125
Pakistan	361 039
Romania	398
Russia	10 747 885
Spain	255
Sweden	41 570
Switzerland	55 329
Tajikistan	83 876
Turkey	25 085
United States	57 482
Uzbekistan	6108

Supplementary Table 4: Population with railway access by country: A spatial analysis based on WorldPop data and 1-degree grid cells

Country	Population
Austria	15 653
Canada	194 960
China	5 108 698
Finland	22 151
France	7572
Germany	240
Italy	2517
Kazakhstan	9486
Liechtenstein	97
Mongolia	815 586
North Korea	24 240
Norway	21 047
Russia	8 915 035
Sweden	35 345
Switzerland	41 194
United States	41 556

Supplementary Table 5: Soil stratigraphy and volumetric composition of soil layers above the natural ground surface in the road embankment, parameter values from ref.3

Depth (m)	Initial water/ice content	Mineral	Organic	Porosity
Road centre				
[0.0, 0.1]	0.15	0.8	0.0	0.2
[0.1, embankment base]	0.2	0.7	0.0	0.3
Road shoulder				
[shoulder surface, embankment base]	0.2	0.7	0.0	0.3
Road toe and remote tundra				
[natural ground surface, peat layer base]	0.7	0.05	0.2	0.75

Supplementary Table 6: Soil stratigraphy and volumetric composition of soil layers above the natural ground surface in the railway embankment, parameter values from ref.4

Depth (m)	Initial water/ice content	Mineral	Organic	Porosity
railway centre				
[0, ballast layer base]	0.0	0.0	0.0	0.44
[ballast layer base, embankment base]	0.1	0.75	0.0	0.25
railway berm				
[ballast layer base, embankment base]	0.1	0.75	0.0	0.25
railway crushed rock				
[ballast layer base, crushed rock thickness]	0.0	0.0	0.0	0.44
[crushed rock thickness, embankment base]	0.1	0.75	0.0	0.25
railway shoulder				
[shoulder surface, shoulder crushed rock thickness]	0.0	0.0	0.0	0.44
[shoulder crushed rock thickness, embankment base]	0.1	0.75	0.0	0.25
Railway toe and remote tundra				
[natural ground surface, peat layer base]	0.7	0.05	0.2	0.75

Supplementary Table 7: Overview of datasets used for simulation

Variable	Datasets	Reference/Source	Comments
Meteorological forcing	ERA5	5	Historical forcing (1950–2023)
Meteorological forcing	MPI-ESM1-2-HR	6	Future forcing (2024–2100)
Volumetric fractions of mineral, organic, porosity, field capacity, and residual water content	Global high-resolution dataset of soil hydraulic and thermal parameters	7–8	Soil stratigraphy
Water table depth	Global water table depth dataset	9	Used to determine initial water/ice content
Bedrock depth	Global bedrock depth dataset	10	Used to constrain soil depth
Geothermal heat flux	Terrestrial heat flow dataset	11	Lower boundary conditions
Four-layer soil temperature	ERA5	5	Initial soil temperature
Geopotential	ERA5	5	Used to calculate the elevation for each grid cell
Peaty soil thickness	Northern peatland maps	12	Used to modify the upper soil stratigraphy of the natural ground

Supplementary Table 8: Overview of parameters used for ensemble simulations in CryoGridLite

Parameter	Symbol	Value/Range	Unit	Source
Natural constants				
Atmospheric pressure at sea level	p	1.005×10^5	Pa	—
Gravitational acceleration	g	9.81	$\mathrm{m\,s^{-2}}$	—
Von Kármán constant	κ	0.4	—	—
Stefan-Boltzmann constant	σ	5.6704×10^{-8}	$\mathrm{W\,m^{-2}\,K^{-4}}$	—
Specific gas constant for air	R_a	2.870 58	$\mathrm{J\,kg^{-1}\,K^{-1}}$	—
Surface properties				
Albedo of fresh snow	$\alpha_{snow,\,max}$	0.85	—	13
Albedo of old snow	$\alpha_{snow,\,min}$	0.50	—	13
Albedo of soil	α_{soil}	0.20	—	13
Albedo of water	α_{water}	0.07	—	13
Albedo of ice	α_{ice}	0.20	—	13
Albedo of the road centre and shoulder surface	α_{road}	0.30	—	3
Albedo of crushed rock	$\alpha_{crushedrock}$	0.28	—	4
Albedo of berm	α_{berm}	0.257	—	4
Emissivity of snow	ε_{snow}	0.99	—	13
Emissivity of soil	ε_{soil}	0.97	—	13
Emissivity of water	ε_{water}	0.99	—	13
Emissivity of ice	ε_{ice}	0.98	—	13
Resistance of snow	$r_{s,\,snow}$	0	$\mathrm{s\,m^{-1}}$	13
Resistance of soil	$r_{s,\,soil}$	50	$\mathrm{s\,m^{-1}}$	13
Resistance of water	$r_{s,\,water}$	0	$\mathrm{s\,m^{-1}}$	13
Resistance of ice	$r_{s,\,ice}$	0	$\mathrm{s\,m^{-1}}$	13
Material properties				
Density of water	ρ_{water}	1000	$\mathrm{kg\,m^{-3}}$	13
Density of ice	ρ_{ice}	1000	$\mathrm{kg\,m^{-3}}$	13
Density of air at sea level	ρ_{air}	1.293	$\mathrm{kg\,m^{-3}}$	13
Evaporation Depth	d_E	0.2	m	—
Volumetric heat capacity of water	C_{water}	4.2×10^6	$\mathrm{J\,m^{-3}\,K^{-1}}$	13
Volumetric heat capacity of ice	C_{ice}	1.9×10^6	$\mathrm{J\,m^{-3}\,K^{-1}}$	13
Volumetric heat capacity of air	C_{air}	1.25×10^6	$\mathrm{J\,m^{-3}\,K^{-1}}$	13
Volumetric heat capacity of mineral soil	$C_{mineral}$	2.0×10^6	$\mathrm{J\,m^{-3}\,K^{-1}}$	13
Volumetric heat capacity of organic soil	$C_{organic}$	2.5×10^6	$\mathrm{J\,m^{-3}\,K^{-1}}$	13
Effective volumetric heat capacity of crushed rock	$C_{crushedrock}$	1.006×10^6	$\mathrm{J\,m^{-3}\,K^{-1}}$	4
Thermal conductivity of water	k_{water}	0.57	$\mathrm{W\,m^{-1}\,K^{-1}}$	13
Thermal conductivity of ice	k_{ice}	2.2	$\mathrm{W\,m^{-1}\,K^{-1}}$	13
Thermal conductivity of air	k_{air}	0.025	$\mathrm{W\,m^{-1}\,K^{-1}}$	13
Thermal conductivity of mineral soil	$k_{mineral}$	3.00	$\mathrm{W\,m^{-1}\,K^{-1}}$	13
Thermal conductivity of organic soil	$k_{organic}$	0.25	$\mathrm{W\,m^{-1}\,K^{-1}}$	13
Effective thermal conductivity of crushed rock	$k_{crushedrock}$	0.346	$\mathrm{W\,m^{-1}\,K^{-1}}$	4
Specific latent heat of fusion water	L_{sl}	0.334×10^6	$\mathrm{J\,kg^{-1}}$	13
Specific latent heat of vaporization	L_{lg}	2.501×10^6	$\mathrm{J\,kg^{-1}}$	13
Grid cell-specific parameters				
Density of snow	ρ_{snow}	[100, 500]	$\mathrm{kg\,m^{-3}}$	—
Maximum snow cover depth	$d_{snow,\,max}$	[0.1, 2.0]	m	14
Height of the road embankment above the natural ground surface	$EBHag_{road}$	[1.5, 15]	m	—
Height of the road embankment below the natural ground surface	$EBHbg_{road}$	[0, 1.5]	m	—
Height of the railway embankment above the natural ground surface	$EBHag_{railway}$	[1.5, 5]	m	—
Height of the ballast layer in railway center	$EBHbl$	[0.3, 0.5]	m	—
Embankment slope of road	$EBslope_{road}$	[1/4, 1/1.5]	—	—
Embankment slope of railway	$EBslope_{railway}$	[1/2, 1/1.5]	—	—
Embankment direction	$EBdir$	[0, 360]	°	—
Embankment width of road centre	$EBwidthroad$	[4, 20]	m	—
Embankment width of railway centre	$EBwithrailway$	[1, 3]	m	—
Embankment width of railway berm	$EBwidthberm$	[1, 3]	m	—
Embankment width of toe	$EBwidthtoe$	10	m	—
Embankment width of tundra	$EBwidthtundra$	50	m	—
Crushed rock width of railway shoulder	$CRwidth$	[0.8, 1.6]	m	15
Peat layer thickness	d_{peat}	maximum/minimum values at grid cell resolution	m	12

References

[1] Darin Koblick, Vectorized Solar Azimuth and Elevation Estimation. MATLAB Central File Exchange. `https://de.mathworks.com/matlabcentral/fileexchange/23051-vectorized-solar-azimuth-and-elevation-estimation` (2025).

[2] Tatem, A,J. WorldPop, open data for spatial demography. *Sci. Data* **4**, 170004 (2017).

[3] Schneider von Deimling, T. et al. Consequences of permafrost degradation for Arctic infrastructure – bridging the model gap between regional and engineering scales. *Cryosphere* **15**, 2451–2471 (2021).

[4] Chen, R., Schneider von Deimling, T., Boike, J., Wu, Q. & Langer, M. Simulating the thermal regime of a railway embankment structure on the Tibetan Plateau under climate change. *Cold Reg. Sci. Tech.* **212**, 103881 (2023).

[5] Hersbach, H. et al. The ERA5 global reanalysis. *Q. J. R. Meteorol. Soc.* **146**, 1999–2049 (2020).

[6] Müller, W. A. et al. A higher-resolution version of the Max Planck Institute Earth System Model (MPI-ESM1.2-HR). *J. Adv. Model. Earth Syst.* **10** 1383–1414 (2018).

[7] Dai, Y. et al. A global high-resolution data set of soil hydraulic and thermal properties for land surface modeling. *J. Adv. Model. Earth Syst.* **11** 2996–3023 (2019).

[8] Dai, Y. et al. Evaluation of Soil Thermal Conductivity Schemes for Use in Land Surface Modeling. *J. Adv. Model. Earth Syst.* **11** 3454–3473 (2019).

[9] Fan, L., Li, H. & Miguez-Macho, G. Global patterns of groundwater table depth. *Science* **339**, 940–943 (2013).

[10] Shangguan, W., Hengl, T., Mendes de Jesus, J., Yuan, H. & Dai, Y. Mapping the global depth to bedrock for land surface modeling. *J. Adv. Model. Earth Syst.* **9**, 65–88 (2017).

[11] Lucazeau, F. Analysis and mapping of an updated terrestrial heat flow data set. *Geochem. Geophys. Geosyst.* **20**, 4001–4024 (2019).

[12] Hugelius, G. et al. Large stocks of peatland carbon and nitrogen are vulnerable to permafrost thaw. *Proc. Natl. Acad. Sci. U. S. A.* **117**, 20438–20446 (2020)

[13] Westermann, S. et al. Simulating the thermal regime and thaw processes of ice-rich permafrost ground with the land-surface model CryoGrid 3. *Geosci. Model Dev.* **9**, 523–546, 2016.

[14] Langer, M. et al. The evolution of Arctic permafrost over the last 3 centuries from ensemble simulations with the CryoGridLite permafrost model. *Cryosphere* **8**, 363–385 (2024).

[15] Niu, F. et al. Long-term thermal regimes of the Qinghai-Tibet Railway embankments in plateau permafrost regions. *Sci. China Earth Sci.* **58**, 1669–1676 (2015).